The source motion of 2003 Bam (Iran) earthquake constrained by satellite and ground-based geodetic data

M. Peyret, J. Chéry, Y. Djamour, A. Avallone, F. Sarti, P. Briole, M. Sarpoulaki

Geophys. J. Int. (2007) **169,** 849–865 doi: 10.1111/j.1365-246X.2007.03358.x

The source motion of 2003 Bam (Iran) earthquake constrained by satellite and ground-based geodetic data

M. Peyret,[1] J. Chéry,[1] Y. Djamour,[2] A. Avallone,[3] F. Sarti,[4] P. Briole[5] and M. Sarpoulaki[2]

[1] *GM: Géosciences Montpellier, UMR 5573, Université de Montpellier II, France. E-mail: peyret@dstu.univ-montp2.fr*
[2] *NCC: National Cartographic Center, Tehran, Iran*
[3] *INVG: Instituto Nazionale di Geofisica e Vulcanologia, Grottaminarda (AV), Italy*
[4] *ESA: European Space Agency, Frascati, Italy*
[5] *IPGP: Institut de Physique du Globe, Paris, France*

Accepted 2007 January 11. Received 2007 January 11; in original form 2005 December 26

SUMMARY

The interpretation of coseismic surface deformation measurements through inversion techniques is of major importance to understand the mechanical behaviour of a seismic fault. Dense geodetic data sets in the vicinity of the ruptured fault provide unique constraints on detailed fault geometry and slip distribution at depth, making them complementary to seismological data.

Bam earthquake (Mw 6.6, 2003 December 26) induced surface deformation has been precisely mapped by Envisat ASAR interferometry and by subpixel correlation techniques applied to Spot-5 and ASAR amplitude images. These oblique and horizontal estimations of deformation have been completed with one levelling profile along the main road crossing the rupture from west to east.

We process these data (separately and jointly) in a two-step inversion technique, within the elastic half-space theory framework. Our objective is to determine the dislocation model at depth that satisfies simultaneously all the geodetic constraints. Also, we estimate the relative contribution of each geodetic data set to this inversion process. We first use a stochastic direct approach called neighbourhood algorithm in order to estimate the average characteristics of the rupture, and their relative uncertainty. Constraining in this way the geometry of the ruptured fault, we then linearize the inverse problem and compute the slip distribution on the fault using a standard weighted least-square technique, assuming the solution is smooth to some degree. At each step, we discuss the optimal models, their stability as well as the relative influence of each data set on the derived models parameters.

Our preferred model reveals a shallow dislocation on a quasi-vertical fault, slightly dipping towards east. The slip vector has a strike-slip component as high as 2 m, while the dip-slip component seems negligible. However, the estimation of the resolution matrices emphasizes the fact that the details of deep fault slip distribution remain out of the scope of this ill-conditioned inverse problem. Yet, our preferred model suggests a main dislocation limited at depth between 1 and 6 km. By contrast, the aftershocks observed in the months following the earthquake are located just beneath the estimated main shock.

Key words: Bam, geodetic data inversion, Iran, levelling, neighbourhood algorithm, SAR interferometry, subpixel correlation offsets.

1 INTRODUCTION

The rupture process of an earthquake can be observed and quantified by several means: seismology, geodesy and field observations. Each technique provides partial insights of the rupture mechanism. Since the end of the 1970s, teleseismic waves are used to infer first-order characteristics of the event. More details (spatial distribution of slip, rupture velocity) can be inferred from near-field strong ground motion records in a well-instrumented area (Archuleta 1982; Olson & Apsel 1982; Hartzell & Heaton 1983; Archuleta 1984). However, this is hardly the case and dense geodetic measurements of the surface deformation (GPS, InSAR and subpixel correlation methods) complement efficiently seismological data, even though they do not contain any temporal information of the rupture process. Geodetic

data give spatial insights on the dislocation at depth, particularly the geometry of the ruptured fault and the slip-distribution along that fault. Of particular importance are estimations of the seismogenic depth that can be compared to the one obtained by aftershocks localization. Since the inversion techniques applied to seismic and geodetic data are instable with non-unique solution, field observations can provide *a priori* constraints that reduce these drawbacks (Jackson 1979).

As for most earthquakes in inland areas since a few decades, geodetic measurements have provided dense information on surface deformation induced by the Bam earthquake, Iran (Mw 6.6, 2003 December 26). ASAR interferograms were constructed from Envisat acquisitions both in ascending, and descending orbits, while horizontal south–north and azimuth offsets were, respectively, computed from 2.5 m Spot-5 THR images and Envisat ASAR complex images. We complete these data sets with an estimation of the vertical coseismic deformation by way of a relevelling survey conducted 40 d after the earthquake by the NCC, along the main road that runs through the ruptured zone from west to east (Motagh *et al.* 2006). Assuming that post-seismic deformation is negligible on the time intervals spanned by measurements, these data sets correspond to different spatial sampling of the same surface deformation projected along different directions.

Different approaches have been developed for processing separately or jointly geodetic and seismic measurements, to infer the geometry of the fault and the spatial distribution of slip. In all cases, estimating source geometry and slip distribution requires a forward model of how crust responds to dislocation at depth. Some authors investigated the effect of vertical or lateral variations in elastic properties (Rybicki 1971; Savage 1987; Arnadottir *et al.* 1991; Eberhart-Phillips & Stuart 1992; Du *et al.* 1994; Pollitz 1996; Savage 1998; Simmons *et al.* 2002; Wang *et al.* 2003; Fialko 2004; Zhao *et al.* 2004; Hearn & Bürgmann 2005). Yet, the most commonly used crustal model, adopted in this study, is the homogeneous isotropic, linear, elastic half-space (Okada 1985).

The major difficulties of this highly non-linear problem are non-uniqueness and instability of the solutions. Derivative-based algorithms offer the most straightforward approach for solving this optimization problem. However, the solution can likely get trapped in local minima and, therefore, highly depends on the initial guess (Arnadottir *et al.* 1992; Jonsson *et al.* 2002; Ward & Barrientos 1986). Generally preferred approaches for estimating the overall dislocation characteristics, like geometry and slip, are derivative-free stochastic direct search for finding models of acceptable data-fit. Among the most important methods, let us cite hybrid downhill simplex Monte Carlo (Clarke *et al.* 1997; Wright *et al.* 1999; Talebian *et al.* 2004), simulated annealing (Delouis *et al.* 2000; Cervelli *et al.* 2001; Salichon *et al.* 2003), neighbourhood algorithm (NA) for (Sambridge 1999a; Lohman *et al.* 2002; Vallée & Bouchon 2004) and genetic algorithm (Hernandez *et al.* 1999). These strategies evaluate data-misfit for a randomly constructed set of models. It is then possible to draw statistical inferences from this ensemble (Sambridge 1999b; Cervelli *et al.* 2001).

So that the detailed slip distribution at depth may be estimated, the inversion problem can be linearized for a fixed geometry. However, additional constraints (smoothness, non-negativity of the model) have to be introduced for restoring the existence, uniqueness and stability of a physically meaningful solution. Within that frame, standard linear weighted least-square inversion procedures have been implemented (Tarantola 1987; Du *et al.* 1992; Arnadottir & Segall 1994; Hudnut *et al.* 1994; Feigl *et al.* 2002; Bos & Spakman 2003; Bos *et al.* 2004; Lovenbruck *et al.* 2004).

We examine in which sense and to which extent the derived dislocation model at depth is well constrained by the input data sets. Do the slip distribution on the fault, the resolution and the reliability of the optimal model change when different data sets are used?

We use here a standard two-step inversion approach (Bürgmann *et al.* 2002; Pedersen *et al.* 2003; Funning *et al.* 2005). The first step consists in the determination of the average earthquake slip by the implementation of the NA (Sambridge 1999a). In addition to that coarse model, this direct search algorithm allows for the statistical analysis of all tested models, which gives clues on the reliability of the optimal model. We use this model to fix the geometry of the fault. Hence, we can use a standard linear weighted least-square inversion method to find slip distribution along the fault that minimizes misfit to measured coseismic displacements. Those displacements misfits are weighted according to estimated measurements errors. Moreover, we decide to impose the slip distribution at depth to be smooth to some degree. All the geodetic data sets can be processed either jointly or separately at both stages. A separate use of the data sets gives insights on their relative influence on the derived model at depth. On the other hand, we expect to derive the most precise and robust model by using them all together.

The paper is organized as follows. We first describe the seismotectonic context of the Bam area, before presenting all the geodetic data available for the Bam earthquake, with some emphasis on the levelling data set. Then, using at first the NA procedure, these data are inverted separately in order to determine their relative power of discrimination over dislocation parameters. We discuss the level of reliability for each parameter. A final coarse model is estimated using the data sets all together. Retaining the geometric characterization resulting from the NA approach, weighted least-square inversions are carried out on these data sets, leading to various slip distribution models at depth. We describe one of them which predict fairly well the surface deformation measurements, while maintaining its roughness to some reasonable degree. We emphasize the poor mid-crustal resolution as revealed by our models resolution kernels. We conclude this paper by comparing our preferred coseismic dislocation model with the observed aftershocks distribution, and presenting the different reasons why our models fail to better predict the observed surface deformation.

2 SEISMO-TECTONIC SETTINGS OF THE BAM EARTHQUAKE

The city of Bam is located east of the southern termination of the Gowk fault, which belongs to the North trending Nayband-Gowk-Sabzevaran strike-slip fault system (Fig. 1). This fault system borders the western edge of the Dasht-e-Lut desert, and connects the Makran accretionnary prism (south) to the deforming belt in Northern Iran (Alborz and Kopet-Dagh). Together with the Neh fault system, located east of the rigid block of the Lut, the Nayband-Gowk-Sabzevaran fault system accommodates the 14 mm yr^{-1} relative motion between central Iran and Afghanistan (Jackson & McKenzie 1988; Walker & Jackson 2002; Vernant *et al.* 2004).

The earthquake of 2003 December 26 in eastern Iran destroyed almost totally the city of Bam, causing a death toll of 40 000 people. Despite its relatively small magnitude (Mw 6.6), this event caused the major natural catastrophe in Iran since the 1990 Rudbar earthquake in northwestern Iran (Mw 7.5) (Gao & Wallace 1995).

Large earthquakes around the Lut block have been reported, and historical earthquakes can be related to the Gowk fault (Ambraseys & Melville 1982; Berberian & Yeats 1999). Moreover, a sequence of

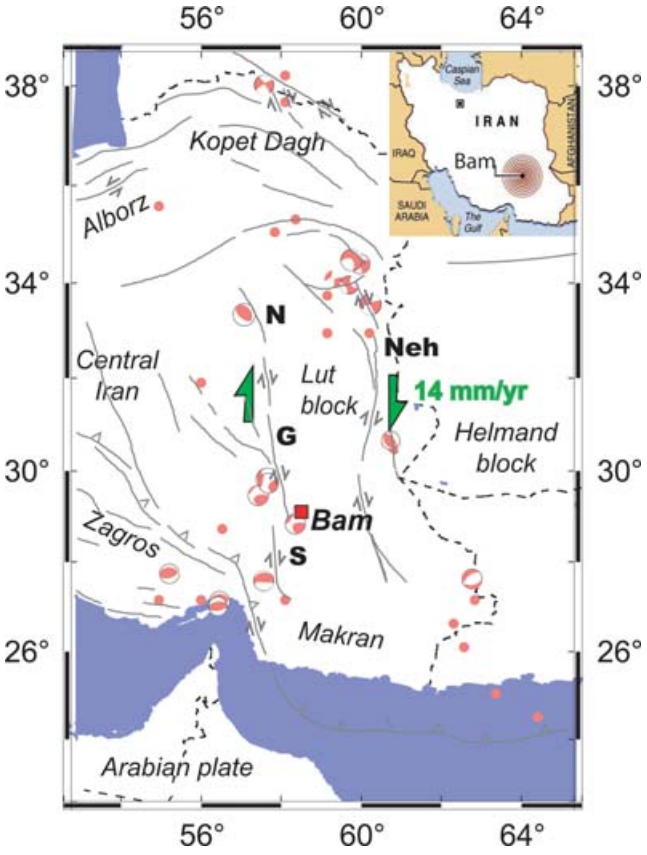

Figure 1. Seismo-tectonic map of Eastern Iran. The convergence of the Arabia and Eurasia plates is accommodated by the Zagros range (south) and the Alborz and Kopet-Dagh ranges (north). The Nayband-Gowk-Sabzevaran strike- slip fault system (N, G and S) connects the Makran accretionnary prism to the deforming belt in Northern Iran. It borders the rigid block of the Lut to the west. Together with the Neh strike-slip fault system, it accommodates the 14 mm yr^{-1} relative motion between central Iran and Afghanistan. Earthquakes location and focal mechanisms are provided by International Seismological Centre Online Bulletin, for magnitude higher than six since 1978. Inset: location of Bam in Eastern Iran.

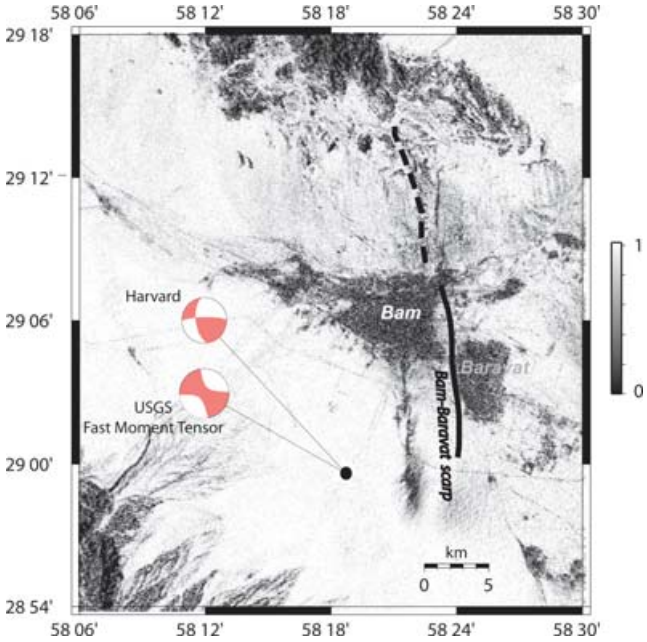

Figure 2. The Bam-Baravat escarpment (black line) and its probable continuation towards north (dotted line) are superimposed to the image of InSAR coherence (descending coseismic interferogram). Black values express loss of radar coherency between the 2 Envisat passes. Geometrical decorrelation, due to the long baseline, can be noticed on the relief north and southwest of Bam. Whereas, temporal decorrelation due to the earthquake is observed on the cities of Bam and Baravat (dwelling that collapsed), and south of Bam, along an 8-km linear structure of en-echelon (right lateral slip) segments of surface breaks. This rupture occurred 5 km west of the Bam-Baravat escarpment. The USGS Fast Moment Tensor and Harvard CMT solution, located 5km west of the rupture, describe the earthquake as a right lateral strike-slip on a quasi-vertical fault trending south–north.

earthquakes ruptured this fault between 1981 and 1998 (Berberian *et al.* 1984, 2001). Yet, neither historical nor instrumental earthquakes have ever been recorded in the Bam surroundings, which explains the good preservation of the 2000-yr-old Bam citadel prior to the 2003 earthquake.

The main shock occurred just below the city of Bam on a hidden (or new) fault branch (Fig. 2). Most of the moment magnitude was released at a shallow depth (about 5 km), but the rupture did not propagate up to the surface. Indeed, very limited surface faulting was found. In agreement with the regional tectonic context, earthquake focal mechanism reveals a rupture on a dextral, vertical strike-slip fault trending north–south. Yet, the dislocation occurred about 5 km west of the Bam-Baravat escarpment, in a place with no topography or drainage features associated with the seismogenic fault.

Even though inversions of geodetic or seismic data agree to say that most of the moment magnitude released at shallow depth, the rupture just slightly broke the surface. This indicates a shallow slip deficit, already reported for earthquakes such as Izmit, Landers or Hector Mine (Fialko *et al.* 2005). Indeed, field observation reports small-scale fissuring along the Bam-Baravat escarpment (probably just induced by shaking) and along a 5 km lineament north of the city. However, the main surface expression of the rupture is located south of the city in the shape of series of discontinuous en-echelon surface breaks, each 50–100 m long (Hessami *et al.* 2004; Fielding *et al.* 2005). They clearly express a dextral motion, with maximum offsets of about 20 cm. The associated surface changes are conspicuous on the coherence channel of the coseismic radar interferograms.

Finally, the analysis of teleseismic *P–SH* body waves together with strong motion records in Bam indicate that a small event (Mw 5.8) occurred about 10 s after the main shock with a reverse faulting mechanism, located further south (Talebian *et al.* 2004; Funning *et al.* 2005). However, aftershocks seismicity does not support the evidence of two distinct faults (Tatar *et al.* 2005). Any how, even though this information should be taken into account in inverting surface displacement measurements, in this study, we restrict ourselves to infer slip dislocation on a single fault.

3 GEODETIC DATA OF THE BAM EARTHQUAKE

The ENVISAT satellite acquired radar images of the Bam area, before and after the earthquake, both in ascending and descending passes, using its 56 mm wavelength sensor. The phase difference between the two combined images contains the variation of the satellite-ground distance during the elapsed time, that is, mainly the coseismic displacement vector projected on the satellite line of sight. Several interferograms can be formed. In this study, we just consider the two coseismic interferograms with the smallest time interval: orbits 9192 and 9693 in descending pass (2003

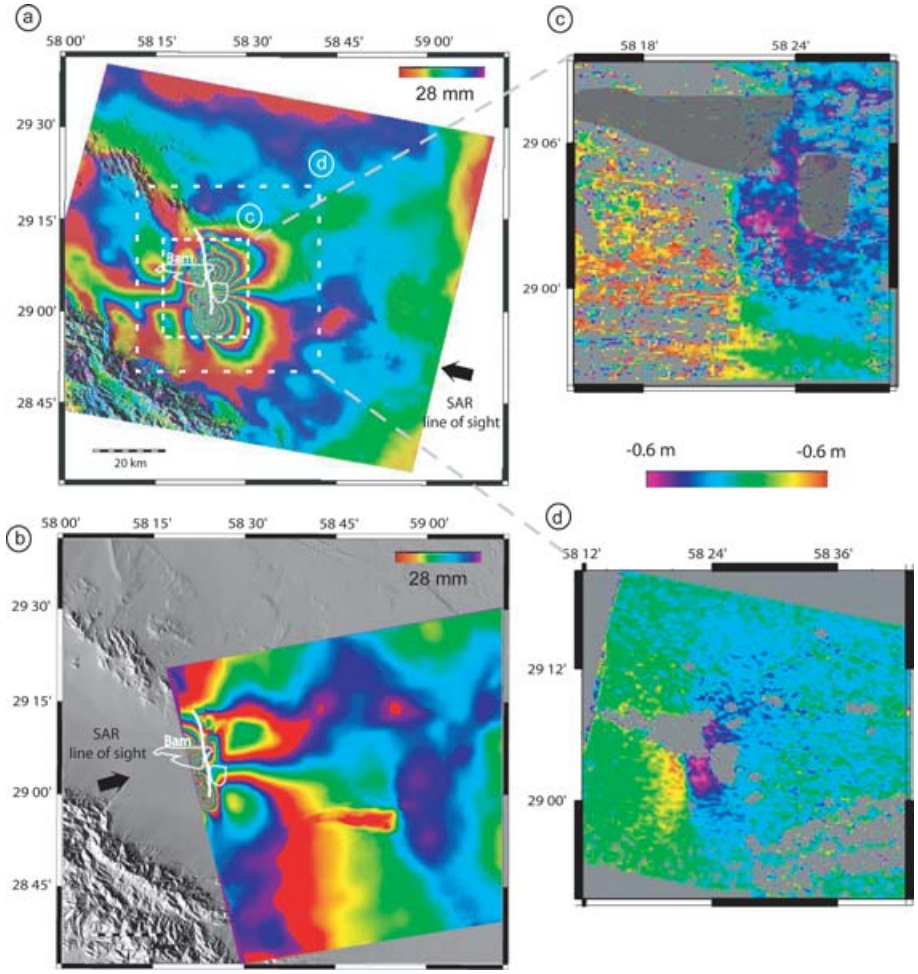

Figure 3. Geodetic measurements of Bam coseismic surface deformation. (a) Coseismic ASAR interferogram in descending orbits (2003 December 03–2004 January 07; $E_a = 20$ m), (b) coseismic ASAR interferogram in ascending orbits (2003 November 16–2004 February 29; $E_a = 1400$ m), (c) N–S offsets derived from Spot-5 THR images (Binet & Bollinger 2005) and (d) N–S offsets derived from ASAR Envisat Complex images (Sarti *et al.* 2005).

December 3–2004 January 7 with a 20 m elevation of ambiguity), and orbits 8956 and 10 459 in ascending pass (2003 November 16–2004 February 29 with a 1400 m elevation of ambiguity) (Figs 3a and b). We correct the original interferograms from the topographic fringes by using the 90 m resolution Shuttle Radar Topography Mission (SRTM) digital elevation model. The remaining fringe system is mainly related to the Bam earthquake motion, even though some atmospheric residuals are present particularly southwest of the city of Bam. Any how, we estimate their amplitude to no more than one fringe, which should not affect significantly the deformation fringe pattern. The spatial resolution is about 20 m, while the precision, depending on the local decorrelation, can be estimated to about 3 mm.

As often in dry continental areas, interferograms have a high quality thanks to minor dielectric changes of the soil properties between the two acquisition dates. The image structure is relatively simple, displaying a four lobes pattern fully compatible with a dextral motion on a north-trending strike-slip fault. This fault is located 5 km west of the Bam-Baravat escarpment. In agreement with field observation and InSAR coherence, phase discontinuity is observed between the lobes south of Bam, where the rupture reached the surface.

InSAR provides direct estimation of satellite line-of-sight deformation component. Due to the 23° elevation angle, its sensitivity is higher for vertical displacement than horizontal. Moreover, the roughly south–north orientation of the fault is poorly adequate to Envisat geometry of acquisition. Indeed, SAR interferometry is poorly sensitive to displacements perpendicular to the SAR line of sight. Hence, we expect the horizontal surface motion close to the rupture to be badly estimated.

A way to complement ASAR interferograms is to estimate the east–west and south–north components of the surface deformation by computing the subpixel offsets between 2 images (optical or radar amplitude) acquired before and after the earthquake. We applied a subpixel correlation method developed by (Michel *et al.* 1999; Michel & Avouac 2002), on two 2.5 m Spot5 THR. A similar processing has been performed on two different Spot5 images (Binet & Bollinger 2005), and also with Envisat ASAR amplitude images (Sarti *et al.* 2005) (Figs 3c and d). The spatial resolution of these techniques depends on the width of the correlation analysis window, typically a few tens of pixels (about one independent estimation every 200 m).

ASAR amplitude offsets have been estimated from 2 Envisat acquisitions separated by a very small baseline. For that, the speckle signature on both images is very similar. This is why the estimated standard deviation is about 10 cm in azimuth and 13 cm in range. The range offset images do not reveal significant spatial changes.

On the contrary, the azimuth component is characterized by a low gradient (10^{-3}) centred on the clearly mapped surface rupture. The amplitude of this deformation is about 0.8 m (up to 1.2 m) distributed over about a 1-km wide deformation zone. This horizontal deformation is significantly higher than the one estimated from ground measurements (0.2 m). Indeed, geologically measured deformation mainly occurs without surface rupture, with just microcracking and small-scale offsets limited to the rupture trace of the fault.

Spot-5 offsets are much noisier. Their precision can be estimated to one tenth of the pixel size, which is about 30 cm. However, they are affected by several biases that make their interpretation more critical, particularly at low frequency. The east–west component does not reveal any significant signal. Nevertheless, the fault localization and orientation (N5°E), as well as south–north offsets amplitude and distribution are similar to those derived from ASAR amplitude offsets.

We also use an estimation of the vertical coseismic surface deformation through levelling (Motagh *et al.* 2006). The main road that crosses the cities of Bam and Baravat from NW to SE belongs to the first order levelling network of Iran. In order to get an estimation of the vertical deformation induced by the Bam earthquake, the NCC performed a levelling survey of this road 40 d after the earthquake. This levelling profile is compared to the previous one performed in 1988 (Fig. 4). The northwestern end of the profile has been set to zero deformation, whereas the eastern end reaches a subsiding zone, as revealed by InSAR over one year of observation (June 03–June 04). This local subsidence is probably due to heavy water withdrawal for irrigation purposes. The levelling profile is 70 km long, with benchmarks every 2 km. Using the 230 levelling lines representing the Iranian first order levelling network, the average precision of this profile is statistically estimated to 1.43 mm $km^{-1/2}$ (Memarzadeh 1998). This could explain the 1 cm vertical discrepancy between east and west null-deformation zone of the profile. Because of the shortness of the profile, the 20 cm relative vertical motion is highly significant, quite above the expected noise level (few mm). Considering the location of this profile, on the northern part of the quadri-lobes deformation pattern, the shape of this profile is consistent with a dextral strike-slip mechanism (upward motion at NW and SE, downward motion elsewhere), even though it does not exclude any thrust component.

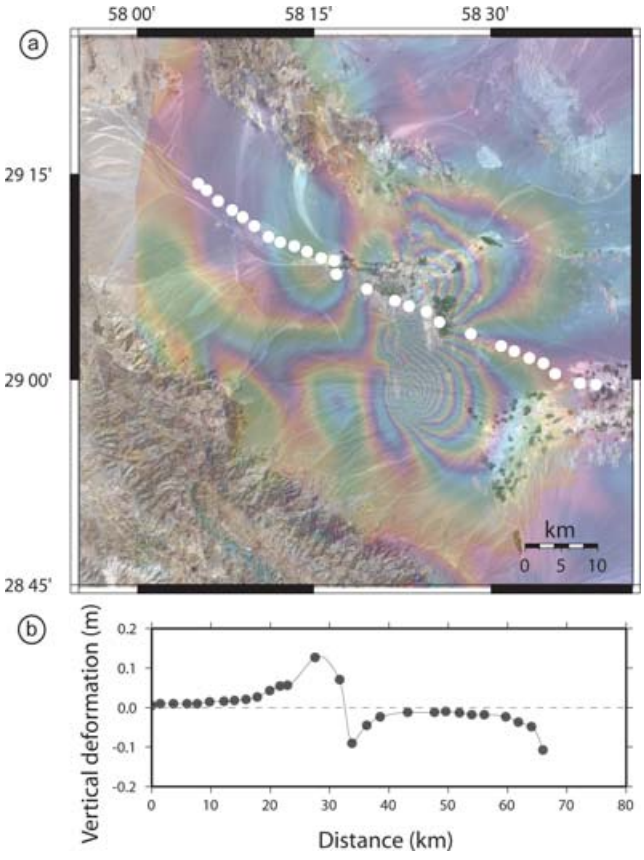

Figure 4. Levelling profile. (a) Localization along the main road and relative position to surface deformation mapped by InSAR. It is long enough to reach the null-deformation zones at both ends. (b) Vertical deformation measured by levelling from NW towards SE. Notice the subsiding zone at eastern end of the profile due to water withdrawal for irrigation purposes.

4 INVERSION PROCEDURE

The inversion problem consists in estimating the characteristics of the dislocation at depth from the geodetic data. What fault geometry and slip distribution can we infer from surface deformation measurements? Such a problem is highly non-linear with non-unique solution.

We present a two-step procedure, making the assumption of a shear dislocation in a uniform elastic earth model, using the Okada analytical solution for deformation (Okada 1985).

Since inversion techniques suffer from a strong dependence on the starting solution, we first try to estimate the overall earthquake motion (geometry, uniform slip) using a stochastic approach: the NA (Sambridge 1999a). Not only this technique determines an optimal model according to a standard misfit function between predicted and observed surface displacement, but it also allows for an estimation of *a posteriori* probability function for all the parameters of the model. However, this last estimate requires an estimate of data covariance. Since data covariance matrices are not well constrained, we simply model our data as independent observations. Under this assumption, the NA process gives insights on the reliability of the optimal model.

This first step allows now to fix the overall geometry of the rupture. Then we can use a standard weighted linear least-square inversion method to find the slip distribution on the fault plane that minimizes misfit to measured coseismic displacements weighted by measurements errors while preserving smoothness of the slip distribution. By this way, we also address the problem of determining how precisely slip distribution models inverted from surface displacement data can be spatially resolved.

Both methods process all available geodetic data sets either separately or all together, using appropriate weighting.

4.1 Determination of the overall earthquake motion by neighbourhood algorithm

The NA is a direct search procedure in the models space with only forward modelling calculation, just as genetic algorithms or simulated annealing. It is a derivative-free search method, particularly well-suited to highly non-linear inversion problems.

The objective is to find a set of dislocation models at depth that preferentially sample the good data-fitting regions of models space, rather than seeking a single optimal model. So we first define the models space, by determining the set of parameters to estimate, and their respective prior boundaries. We limit our study to uniform slip on rectangular fault embedded in a uniform elastic half-space. Each model is defined by 10 parameters: centroid localization, orientation,

width and length of the fault plane, slip vector, and the Poisson's ratio (we assume a Young modulus $E = 80$ GPa). We checked that geodetic measurements are not affected by any constant offset or gradient (null-deformation zones in the far field have deformation estimates equal to zero). These constants could be integrated as additional parameters in the models space.

For each sample in the models space, we use forward modelling and estimate an objective function that measures the discrepancy between observed data and theoretical predictions. We use the following Chi-square misfit function:

$$X_\nu^2(m) = \frac{1}{\nu} \sum_{i=1}^{\text{datasets}} w_i [d_i - g_i(m)]^T C_i^{-1} [d_i - g_i(m)]. \quad (1)$$

For a given model m, the predicted surface deformation projected along each axis of observation $g_i(m)$ is compared to the corresponding measured data d_i . ν is the number of degrees of freedom (number of data minus the number of independently constrained model parameters). Its value is only used ultimately for determining an absolute measure of data fit, since the algorithm just requires models to be assessed for their relative fit to the data. C_i are the data covariance matrices constructed from the corresponding estimation of standard deviation of the noise. The weights w_i are chosen so that the misfit is approximately equilibrated between the different data sets we use. Therefore, we expect the inversion not to be dominated by part of the data. This weighting should reflect our relative confidence on these data. Conversely, we used different weights for increasing the prevalence of one data set over the others, in order to estimate its relative influence on the optimal derived model.

NA makes use of the geometrical constructs known as Voronoi cells to derive the self-adaptative search behaviour in model space (Sambridge 1999a). It generates new samples by resampling chosen Voronoi cells with a locally uniform density. The idea is that the misfit of each of the previously tested models is representative of the region of space in its neighbourhood. In that way, the algorithm concentrates sampling simultaneously in different regions of space where the information appears to be robust.

The algorithm just requires two tuning parameters: for each step of the process, the number of new models generated, and the number of cells to be resampled. Depending on the value of the later parameter, the procedure is essentially exploratory (search for a global minimum) or localized (efficient as an optimizer, but possibly detecting a secondary minima). In our study, at each iteration the NA generates 30 models for the current 25 best models.

It is demonstrated that this procedure is a way of sampling the *a posteriori* probability density function (Sambridge 1999b). We evaluate as many samples as possible and analyze the entire ensemble by evaluating Bayesian integrals. For each parameter, we finally get its optimal value and statistical estimations of its stability.

4.2 Linear least-square inversion of slip distribution along a fixed fault geometry

The NA is supposed to provide us with the main characteristics of the dislocation. We retain the geometry of the fault and the elastic parameter. Since the NA was limited to a fault plane, we could now introduce more complexity to this first-order geometry by defining the fault as a set of as many rectangular patches as we want.

Hence, this second inversion stage estimates the slip distribution over a fixed geometry. We implement a standard linear least-square inversion technique under constraints (known as Penalty Function Technique). The problem to be solved is to find the slip vector (model m) that minimizes the following penalty function

$$Pb : \text{minimize } \mu_{sm} \|\nabla m\|^2 + \sum_{i=1}^{\text{datasets}} \mu_i \|W_i d_i - W_i P_i G_i m\|^2, \quad (2)$$

where G_i are the data kernels (matrices of Okada parameters) which relate slip on individual fault patches to surface 3-D motion at all surface observation points. P_i are the projection matrices onto the corresponding direction of measurement (vertical for levelling, horizontal for offsets, and satellite line of sight for InSAR). W_i are weighting matrices that express the confidence we have for each observation. Moreover, we expect the dislocation model at depth to be smooth to some degree. Such a constraint is important in restoring a stable, physically meaningful solution. The roughness of the estimated slip distribution is expressed by a finite-difference approximation of the Laplacian (∇). The extent to which smoothness is enforced at the expense of fit to surface displacements is controlled by varying the smoothing parameter μ_{sm}. We retain a value which suppresses spurious structure in the slip distribution while not smoothing out salient features.

As for the NA inversion, the influence of each data set on the derived model is controlled by the associated weight in the penalty function. An *a posteriori* optimal choice of these parameters can be made by plotting models on a graph representing their misfits relatively to different data sets (known as Tikhonov plots). We retain the model for which the misfit to all data sets looks the most acceptable.

Hence we can, then, estimate the slip-distribution model at depth:

$$\boldsymbol{m} = \left[\mu_{sm} \nabla\nabla^T + \sum_{i=1}^{\text{datasets}} \mu_i (P_i G_i)^T C_i^{-1} (P_i G_i) \right]^{-1} \times \left[\sum_{i=1}^{\text{datasets}} \mu_i (P_i G_i)^T C_i^{-1} \boldsymbol{d_i} \right]. \quad (3)$$

This inversion procedure allows for the determination of the *a posteriori* model covariance C:

$$C = \left[\mu_{sm} \nabla\nabla^T + \sum_{i=1}^{\text{datasets}} \mu_i (P_i G_i)^T C_i^{-1} (P_i G_i) \right]^{-1} \quad (4)$$

and a model resolution kernel R:

$$R = C \cdot \left[\sum_{i=1}^{\text{datasets}} \mu_i (P_i G_i)^T C_i^{-1} (P_i G_i) \right]^{-1}, \quad (5)$$

which expresses how well resolved is the slip vector on each fault patch.

5 RESULTS

5.1 Data sampling and weighting

Orthorectified ASAR interferograms are filtered using the power smoothing algorithm developed by Zhong Lu and modified by Tim Wright. Then, phase is unwrapped (Ghiglia & Romero 1994) and converted to satellite line-of-sight displacement. Finally, complete interferograms (100 km $\times$ 100 km) are subsampled onto a 100-m regular grid in order to reduce computational cost. Even though some high frequency patterns are lost, particularly along the surface rupture, this sampling respects the main deformation features, as much in far field as close to the rupture.

Neither filtering, nor subsampling are applied to offsets and levelling data. Spot-5 offset images have a 160-m grid resolution, with

one independent measurement every 640 m. ASAR offsets images have been estimated on a 400 m spaced grid in slant-range geometry, then orthorectified onto a 500 m spaced grid.

The inversion procedure described in chapter 4 makes use at both stages of weighting matrices for each geodetic data set. They are *a priori* covariance matrices expressing the confidence we have for each measurement. For InSAR, we use the corresponding coherence estimation which major effect is to remove phase estimation over the cities of Bam and Baravat. For offsets data sets, we process in the same way using the signal-to-noise ratio (SNR) estimated during the correlation processing. However, in the case of Spot-5 offsets, SNR information seems insufficient to characterize the measurements reliability. So, we assign a poor confidence level to the highest offset estimates (typically more than 1.0 m). Finally, we define a constant confidence interval for each levelling measurement, but we remove the eastern end of the profile that is obviously affected by subsidence due to water-withdrawal (at distance higher than 50 km along the profile). The levelling standard deviation, estimated from global Iranian network, is set to 3 mm, which is probably overestimated since there is no topography on this short segment, and that we can fix its endings to zero despite the subsidence pattern that affects the eastern part of the profile.

5.2 Coseismic models inferred by neighbourhood algorithm

In order to test the NA approach, we decide not to impose too constrain full prior boundaries on any parameter, even though direct interpretation of geodetic data sets makes it possible. The two tuning parameters have been selected in order to explore the models space in a way as exploratory as possible, while limiting the computational cost.

The optimal models obtained for each geodetic data set processed separately are presented in (Table 1), with their corresponding rms misfits on all data sets summarized in (Table 2). Moreover, estimations of the *a posteriori* probability density function (PPDF) for each parameter are displayed (Fig. 5). From the 10 parameters defining our models space, we derive estimations of two additional parameters: the upper and lower boundaries of the rupture.

Processing interferometric data sets leads to well-resolved parameters (Fig. 5a). Each PPDF has a single narrow peak. The preferred geometry is a quasi-vertical fault plane dipping slightly towards east, which location is consistent with the observed surface rupture. The slip vector has a 2.5 m right lateral strike-slip component, with a null thrust component. The main rupture is limited to a 10-km long segment, which width is evaluated to about 6 km. Such a model leads to a geodetic moment equal to 5×10^{18} N m, which is consistent with seismology (USGS Fast Moment Tensor or Harvard CMT solution). All NA optimal models presented subsequently have similar geodetic moments.

Table 2. Misfit estimations (in cm) of all geodetic measurements for each dislocation model estimated either from one single surface deformation dataset, or combining all geodetic datasets and using Neighbourhood Algorithm (NA) or Weighted Least-Square (WLS) technique.

	InSAR desc/asc	Levelling profile	ASAR offset	SPOT offset
InSAR model	1.6/1.5	2.3	10.7	12.0
Levelling model	3.1/2.2	1.0	11.0	12.0
ASAR offset model	3.2/1.6	4.5	10.2	12.5
SPOT offset model	2.9/1.6	2.9	10.6	10.5
Global NA model	1.7/1.6	1.8	10.6	11.6
WLS model	1.8/1.6	1.5	10.5	11.2

The predicted descending interferograms and their corresponding residues are presented (Fig. 6a). The rms for descending and ascending interferograms are 1.5 and 1.4 cm, respectively. This is about the same as found by (Wang *et al.* 2005) with a more complex geometry and varying slip distribution along the fault. The phase residues are mainly located in a 10-km wide zone centred on the rupture. Surprisingly, we obtain a very good fit for the levelling profile, even though it was not used for guiding the NA process (Fig. 6b). The rms for levelling is estimated to 2.2 cm (4.4 cm using Wang's model). This probably expresses the fact that the radar elevation angle is well adapted to vertical ground motion detection. Precisely, it is not the case for the south–north horizontal component of surface deformation. Yet, offsets misfits (10.7 and 12.0 cm for ASAR and Spot data, respectively) are in the order of measurements uncertainties (Fig. 6c). The mean offset variation across the rupture is estimated to 0.8 m, in agreement with offset observation. However, the analysis of offset residues reveals that this dislocation model fails to predict small-scale horizontal gradient close to the fault. May be this can be explained by phase discontinuities across the fault, local loss of coherence and unwrapping underestimation of ground motion. So, except very close to the rupture, InSAR alone seems sufficient to

Table 1. Model parameters for the Neighbourhood Algorithm. For each parameter, columns 2 and 3 define the prior imposed boundaries, while the following columns show the optimal values obtained when using respectively, InSAR, Levelling, ASAR offset, Spot5 offset measurements and finally all of them together.

Parameters	Min	Max	Optimal InSAR	Optimal Levelling	Optimal ASAR Offset	Optimal Spot5 Offset	Global model
X_c(km)	622	642	631.85	631.72	632.05	631.50	632.00
Y_c(km)	3200	3230	3213.90	3217.55	3213.61	3213.35	3215.30
Z_c(km)	−8	−2	−5.80	−5.37	−2.83	−5.34	−4.8
Length (km)	5	30	10.05	22.67	27.58	16.14	12.1
Width (km)	2	8	5.70	7.18	2.60	4.5	5.6
strike (deg)	−10°	15°	−0.4°	−1.1°	−4.0°	−9.2°	1.6°
dip angle (deg)	60°	110°	86°	97°	92°	103°	88°
Poisson's ratio	0.15	0.3	0.21	0.22	0.28	0.19	0.20
strike slip (m)	−3.0	1.0	−2.53	−1.62	−2.00	−2.45	−2.00
dip slip (m)	−1.0	1.0	−0.01	−0.41	0.19	−0.57	−0.32
Z_{top} (km)	−6	0	−2.5	−1.9	−1.8	−3.1	−2.2
Z_{bottom} (km)	−12	−4	−7.3	−8.2	−4.1	−7.6	−7.0

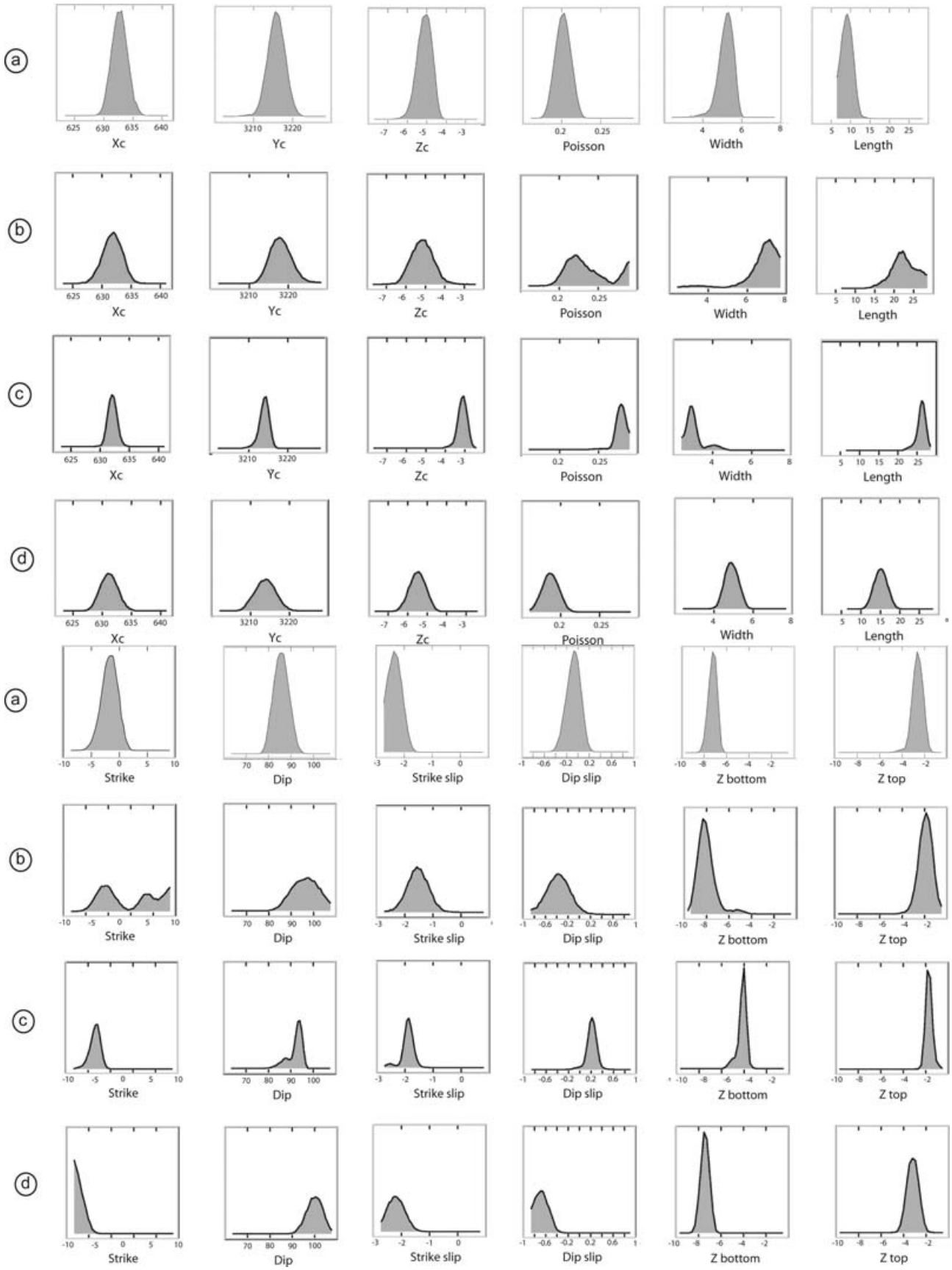

Figure 5. 1-D marginal distribution for the 10 parameters defining the model space and 2 additional parameters: top and bottom of the rupture. Geodetic data sets are processed separately. (a) Descending and Ascending ASAR interferograms, (b) Levelling profile, (c) ASAR offsets and (d) Spot5 offsets.

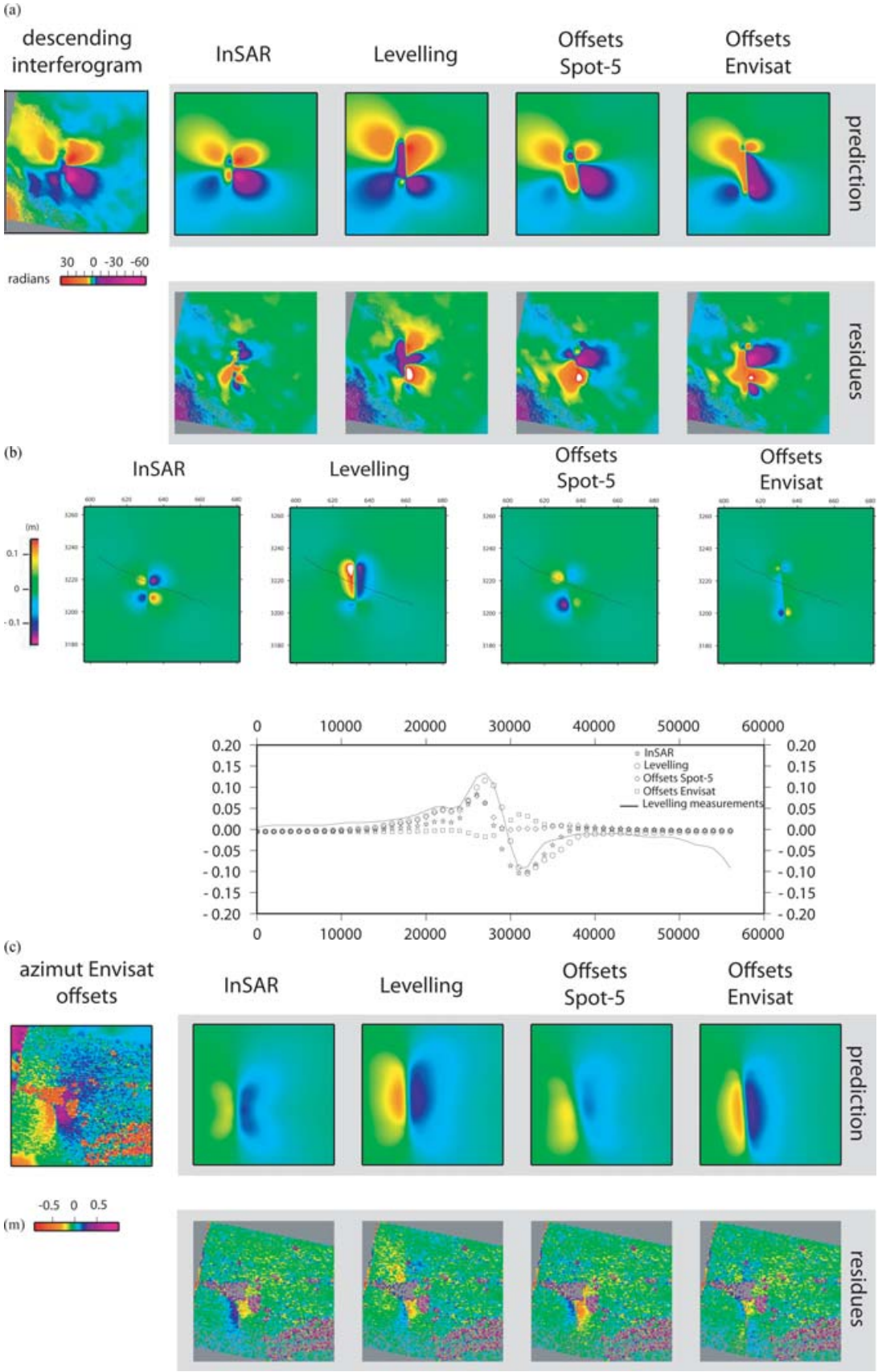

Figure 6. For each geodetic data set processed separately with NA, we present surface deformation prediction and residues for (a) descending ASAR interferogram, (b) vertical deformation prediction and levelling profile and (c) south–north horizontal deformation and ASAR offsets.

derive a coarse dislocation model that predicts fairly well as well horizontal as vertical surface deformation. An increase of phase sampling does not change significantly these results.

The minimization of levelling misfit alone, leads to an optimal model not so different from the one derived previously (Fig. 5b). However, main differences can be noticed. At first, the solution is globally poorly constrained. This is expressed by large confidence intervals associated with most parameters. Especially some geometrical characteristics of the rupture appear to be impossible to constrain with levelling. Indeed, our single profile is roughly perpendicular to the fault. Consequently, it can not provide any unambiguous information about fault length and strike. Residues on Envisat offsets reveal that, although the horizontal surface motion is well predicted in the neighbourhood of the levelling profile, it is not the case north of Bam (Fig. 6c). This proves that the rupture length is overestimated, but reinforces the estimation of a shallow dislocation since, by contrast with InSAR, this model predicts small-scale gradient close to the fault. In other respects, one single levelling profile is obviously insufficient for deciding of a trade-off between strike-slip, dip-slip and depth boundaries of rupture contribution to vertical surface displacement. These uncertainties are revealed by the PPDF flatness or ambiguity for the corresponding parameters. Nevertheless, the optimal model suggests a significant vertical slip component along a quasi-vertical fault plane, dipping towards west, which differs slightly from model derived from InSAR data. Indeed, the south–north symmetry observed on the interferograms is inconsistent with significant dip-slip (Fig. 6a). Despite these differences, mitigated by their associated confidence, the levelling profile appears compatible with the dislocation model derived from InSAR.

The south–north offsets component supplies reliable information on fault location, and provides unique information on horizontal motion. The NA optimal model derived from ASAR offsets (Fig. 5c) confirms the fault location and orientation as described by (Sarti *et al.* 2005). On the contrary, dip angle and fault width are poorly constrained. Yet, the top of the rupture seems to be steadily estimated to about 1.6 km. This is a little deeper than suggested by (Sarti *et al.* 2005), but remains very shallow. However, contrary to all other models, the lower part of the rupture is located at only 4 km, compared to the depth of about 7 km generally estimated, but once again the associated confidence interval is large. In other respects, probably correlated with fault width uncertainty, strike- slip amplitude is estimated to 2.0 m with a large confidence interval suggesting a possible higher slip value. The main rupture length is estimated to more than 20 km, which is quite more than the 12 km retained by authors. This can be explained by the presence of decorrelated and small deformation gradient zones in the northern part of the rupture. Finally, let us notice that the suggested normal component is invalidated by interferograms and levelling measurements.

The optimal model derived from Spot-5 offsets (Fig. 5d) is consistent with previous models. Surprisingly, the strike angle is higher than the expected one (N5°E). Such a misestimate must be attributed to the presence of large low-confidence areas close to the rupture, particularly northwest of the studied zone, and likely erroneous offset estimates south of the rupture. The upper boundary of this model is significantly deeper than the previous ones. It means that it is more sensitive to large scale deformation than high gradients close to the rupture which are affected by significant noise. As for levelling, this model suggests a possible small thrust component. However, as for most parameters, the confidence interval is large.

The conclusion we draw from these separated inversions, is that they all converge towards similar models. However, InSAR data seem to carry the richest and most reliable information. Levelling and offset data, providing reliable ground deformation measurements close to the fault, complement significantly InSAR model by suggesting a shallower dislocation. We process all the data sets jointly, weighting each misfit function according to the data measurement uncertainty and data spatial density. These final model characteristics are presented in Table 1, Table 2 and Fig. 7. In prospect of comparing these models to aftershocks distribution, it is worthy noting that all models limit the main rupture between 1 and 8 km, apparently excluding any deeper dislocation.

5.3 Slip distribution models at depth

Thanks to the NA approach, we are now able to propose a reliable coarse geometry of the rupture. Imposing such an *a priori* fault geometry allows for the linearization of the inverse problem. The objective of this second processing is to investigate the possibility of a varying slip vector along the fault.

The geometry of the NA optimal model is extended laterally and at depth in order to reach the null-deformation zones. Allowing so, slip at higher depth may lead to higher geodetic moments. Indeed, further presented models have geodetic moment estimated to about 20×10^{18} N m, which is significantly higher than seismic moment. The fault plane is divided into small plane patches which extend is about 2 km along strike, and 3 km along the dip angle (with a geometrical ratio with depth). Later discussion on the resolution matrices reveals that finer discretization of the fault plane is useless.

The general inversion problem (eq. 2) is solved for a wide range of weighting coefficients. The rms for each data set misfit is estimated for every model. The best fit is obtained for each data set taken separately, if a high roughness is admitted. However, this could be an unrealistic choice. In order to get an idea of admissible slip gradients along the fault, let us consider the relationship between static-stress drop $\Delta\ \sigma$ and mean slip u for a uniform stress-drop shear crack (Aki 1972; Scholtz 1990):

$$\Delta\sigma = C\mu\left(\frac{\Delta u}{\Delta}\right) \tag{6}$$

C is a constant depending on the geometry of the rupture (set to 1); μ is the shear modulus and Λ the characteristic dimension of the rupture. It has been proposed that stress drop varies strongly with position and high frequencies in slip distribution can be sometimes admissible (Bouchon *et al.* 1998). However, it is likely that the maximum stress drop does not exceed 100 MPa because it would cause the brittle failure of the surrounding crust. Therefore, assuming a maximum static-stress drop of 100 MPa and a mean slip of 1 m leads to a characteristic rupture length of 0.3 km. This maximum dislocation gradient is guaranteed by imposing a corresponding dislocation roughness. A second criterion for roughness admissibility is the importance of backward slip in our models. Since we decide not to impose any positivity constraint, our models can reveal such pattern. By selecting low slip roughness we limit the amplitude and the spatial distribution of these unacceptable backward slips. So, the use of Tikhonov plots (concurrent rms of all geodetic data set misfits) allows for the choice of a preferred set of weighting coefficients, consequently of a derived model of rupture at depth. This model is supposed to predict reasonably well all the surface deformation measurements together.

Our preferred model is presented (Fig. 8). It is fully consistent with previously derived NA models and does not reveal new major heterogeneity that would have been missed by these models. It confirms that the main dislocation is limited at depth between 1 and

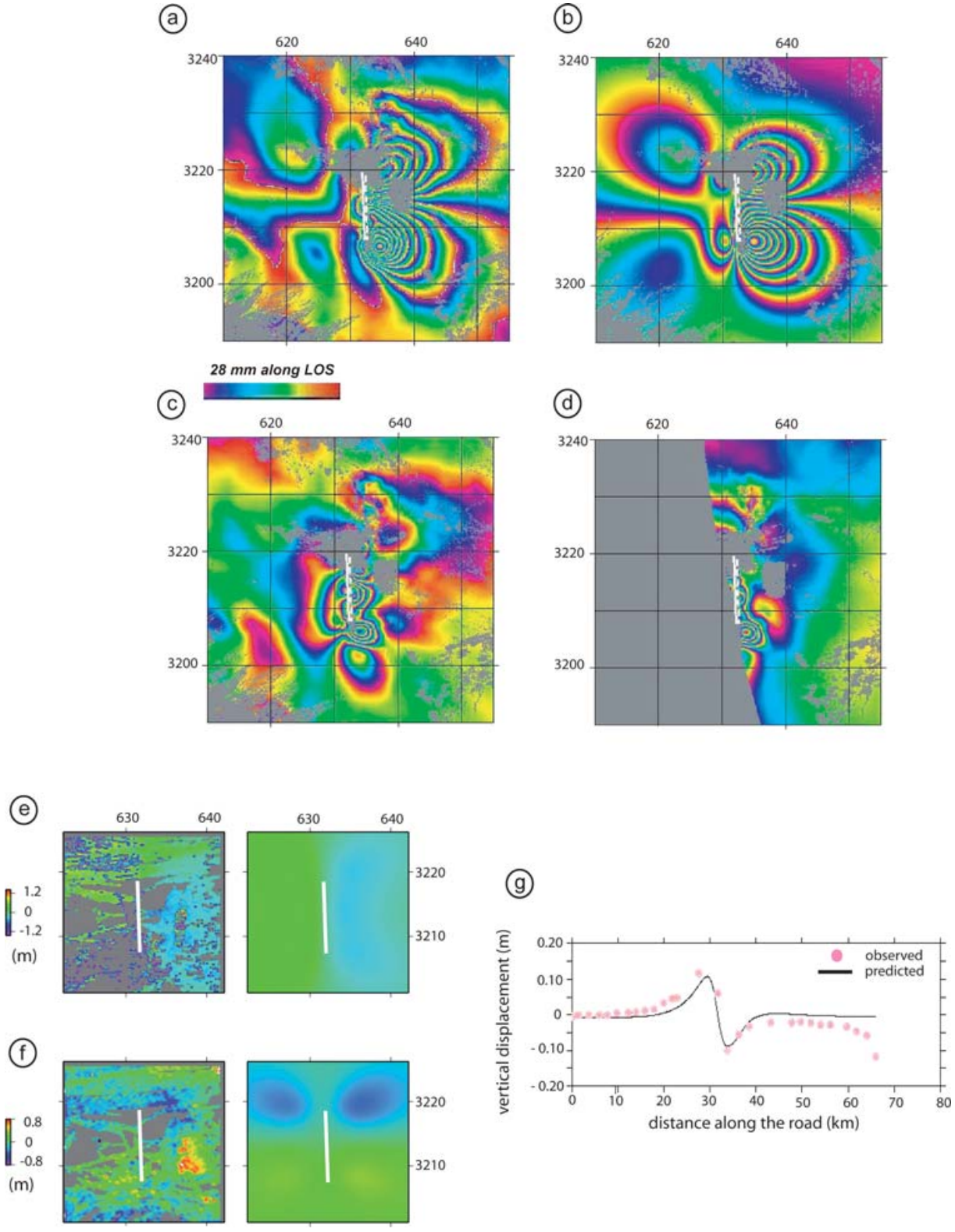

Figure 7. Data misfit for the optimal model computed from InSAR by the Neighbourhood Algorithm. The fault geometry is plotted in white. Its location is consistent with field observations and InSAR loss of coherence. (a) Real descending interferogram (b) simulated descending interferogram (c) residual descending interferogram. The residues are mostly located in a 10 km wide zone centred on the fault. The residues located southwest may be attributed to atmospheric artefacts. (d) Residual ascending interferogram. The main residues are observed at the southern end of the modelled fault. (e) S-N Offset estimated from SPOT5 images (left) and predicted by the model (right) (f) E–W Offset estimated from SPOT5 images (left) and predicted by the model (right) (g) levelling observations (red circles) and predictions (black line). Even though levelling data were not used in this model estimation, the predicted levelling profile fits very well the observations. The rms is 2.2 mm, excluding the subsiding zone at eastern ending of the profile.

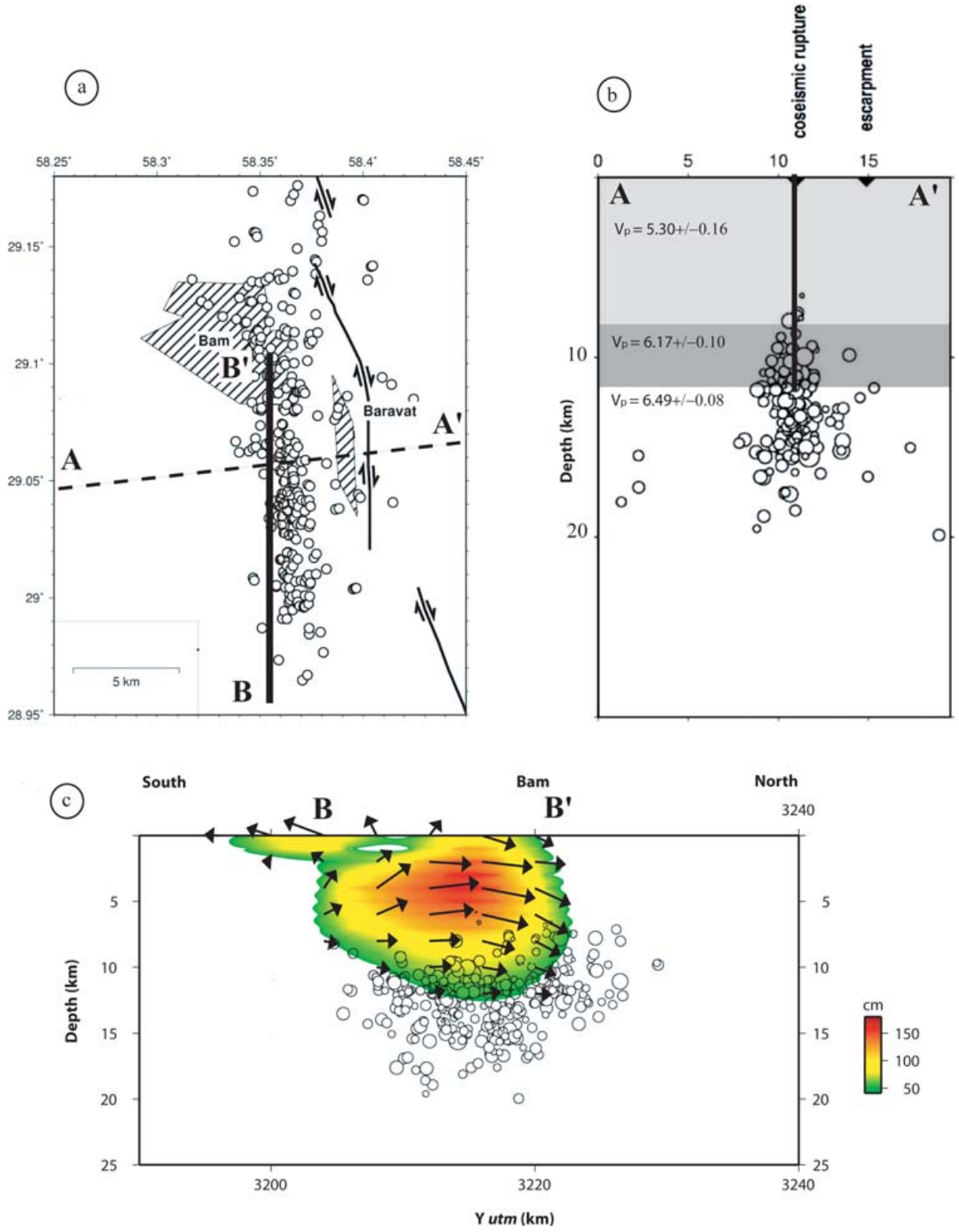

Figure 8. Slip distribution along the fault superimposed to aftershocks location (Tatar *et al.* 2005). (a) The main dislocation (segment BB′) is limited to a 15 km long segment, south of Bam, 4 km west of Bam-Baravat escarpment. (b) The quasi-vertical fault is mapped on aftershocks location along the cross section AA′. The main rupture occurs at depth between 1 and 6 km, and becomes null at about 12 km. The highest aftershocks density corresponds to the deepest end of the main dislocation. A three-layer velocity structure model proposed by (Tatar *et al.* 2005) is displayed. Since the main rupture occurs within a single layer, this justifies our hypothesis of a uniform elastic half-space. However, we suggest exploring the possibility of horizontal or lateral variations of elastic properties in order to explain surface deformation modelization residues. (c) The slip distribution along the fault, with a maximum of 1.8 m at a depth of 5 km. An increase of model roughness results in a more heterogeneous dislocation model, and a higher slip amplitude. Notice the backward slip zone south of the main rupture. Aftershocks are located just below the estimated main shock.

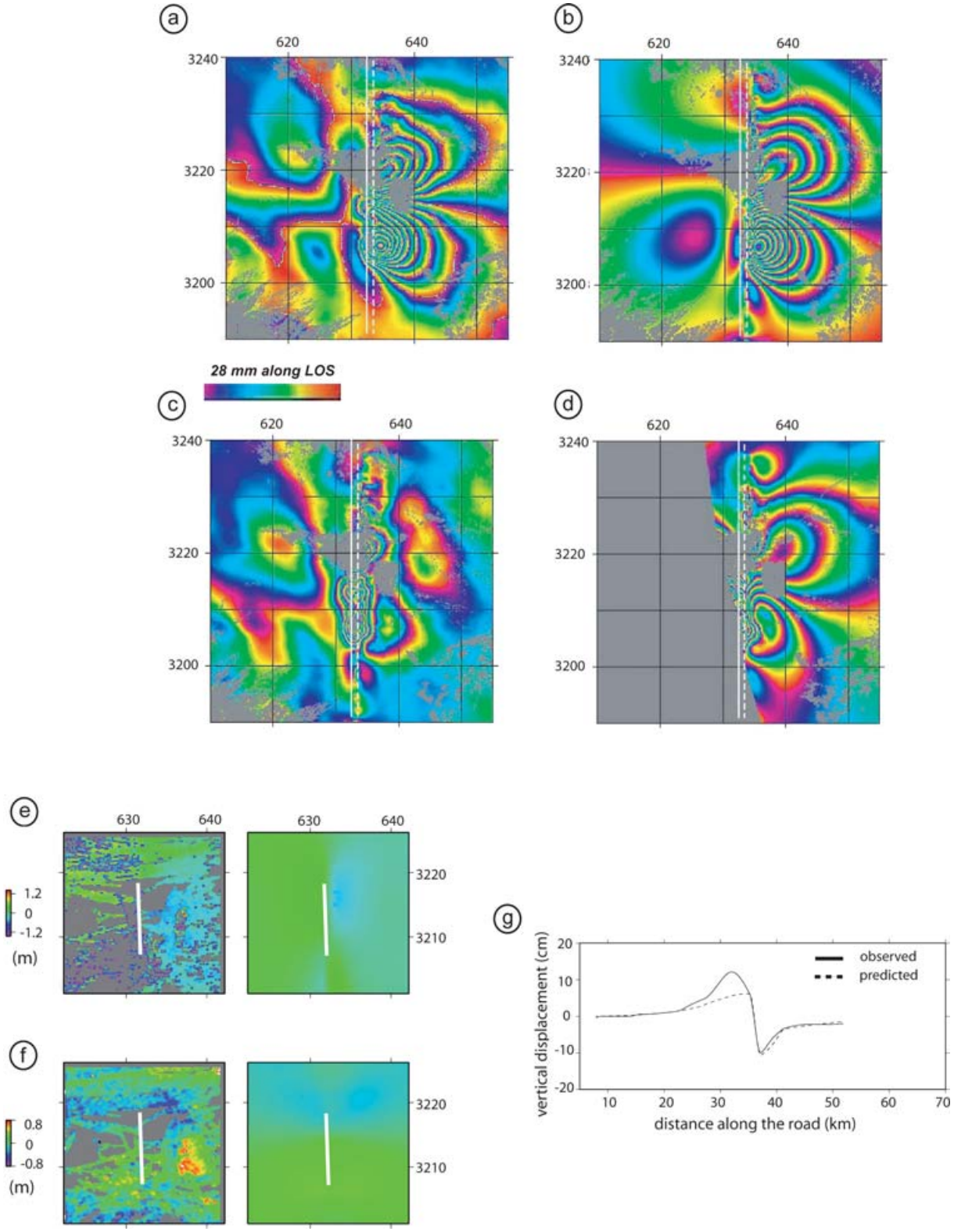

Figure 9. Data misfit for our best model derived by linear least-square inversion. (a) Real descending interferogram, (b) simulated descending interferogram, (c) residual descending interferogram, (d) residual ascending interferogram, (e) S–N offset estimated from SPOT5 images (left) and predicted by the model (right), (f) E–W offset estimated from SPOT5 images (left) and predicted by the model (right) and (g) levelling observations and predictions.

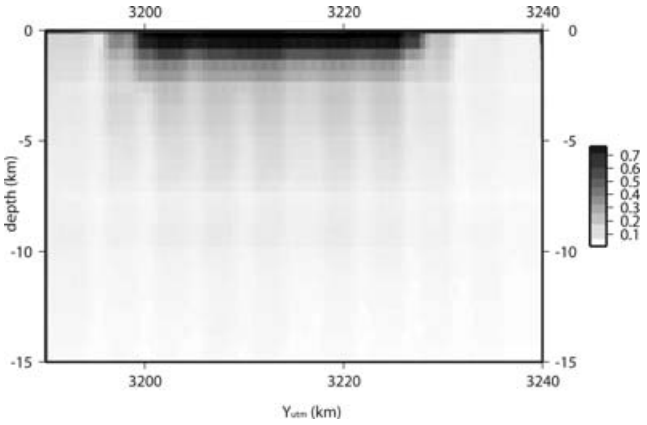

Figure 10. Resolution matrix for a given roughness weighting using all geodetic data sets. Offset and InSAR guarantee a good resolution on slip distribution on the first 5 km. This resolution decreases dramatically deeper. Levelling increases the resolution in its vicinity (around $Y = 3220$ km).

6 km, with a maximum right-lateral slip component of about 1.8 m (up to more than 2.5 m in some less smooth models). The slip amplitude falls down to less than 1 m below 6 km. The thrust component is lower than 0.5 m. The main rupture occurred within a 15 km long segment, south of Bam.

This model is consistent with the geometry and the right-lateral slip revealed by offsets images. Moreover, the rms for the descending interferogram is estimated to 1.4 cm, and 1.6 cm for the levelling profile (Fig. 9). The phase residues are now concentrated close to the rupture (the lower is the model smoothness, the narrower is the band of phase residues). Relaxing the constraint on levelling misfit starts by degrading the vertical estimations located close to the rupture towards the west, while the rest of the profile remains correctly estimated. This expresses the prevalence of other geodetic data sets over levelling in the vicinity of the rupture, and their relative incompatibility. This discrepancy could be attributed to local unwrapping problem or atmospheric artefacts in InSAR data. Considering the set of models that we tested, it seems difficult to obtain a significant better fit for all the data sets together. Lastly, let us notice a backward slip zone located in the southern part of the rupture. Since we did not impose any *a priori* positivity constraint, such a pattern likely reveals some local geometrical changes of the fault or localized artefacts in data.

We decided not to impose external constraints on derived models except smoothness, in order to be able to easily estimate the associated resolution kernels even though it is possible to do so with additional constraints (Du *et al.* 1992). Moreover, since slip positivity should be implicit in geodetic data, any backward slip in the dislocation model will reveal local artefacts in the inversion procedure. The interpretation of these artefacts should help to define a more accurate slip model. The model resolution is estimated by equation (eq. 5), and presented (Fig. 10) for the smoothness coefficient adopted for our 'best model'. The lower is the model roughness, the lower is the resolution since it introduces a spatial dependency of model parameters. It reveals that the resolution of slip distribution models at depth larger than a few km, typically 5 km, is very poor. We tested that an increase in data density only improves the resolution at upper crustal levels. This very poor resolution of the mid-crustal levels is inherent in the inverse problem of retrieving fault slip from surface deformation data using elastic dislocation theory, which is intrinsically ill-conditioned. So, using the elastic dislocation theory for inverting geodetic data restricts us just to the overall motion characteristics, particularly deeper than just a few km.

6 DISCUSSION

The NA analysis of each geodetic data set revealed their complementarities. Interferograms provide the most dense and reliable information, but fall down on estimating the deformation gradient close to the fault. Offsets images fill that gap when SNR is acceptable, while levelling acts the same but with a much reduced scope. A joint analysis of these data sets leads to a reliable estimation of the overall main shock characteristics. Retaining the fault geometry, the weighted least-square inversion process allows for a finer spatial determination of slip within the shallow part of the seismogenic crust. The misfit between the optimal model surface deformation prediction and geodetic data sets is not significantly improved. Also, the main dislocation features reveal some backward slip zones that could be related either to poor local geometry modelization, or to the local influence of atmospheric artefacts in interferograms.

The coseismic models presented in this paper provide insights on mechanism of accumulation and release of stress and strain in the shallow seismogenic crust. Therefore, they should be consistent with aftershocks distribution. Indeed, aftershocks are expected in areas of coseismically induced stress increase (Das & Henry 2003), either along the main fault (at local heterogeneities or ends of the main rupture), or off the fault where the Coulomb failure criteria is reached.

Seismological surveys were performed, right after the earthquake, using dense seismological networks (Nakamura *et al.* 2005; Tatar *et al.* 2005). In agreement with coseismic geodetic data, all recorded events are distributed along a 20 km long, north–south trending cluster, and 5 km west of the Bam-Baravat escarpment. They are mainly located at depth between 8 and 18 km, just beneath the fault segment that, according to our models, experienced the maximum slip (Fig. 8). The velocity structure estimated by (Tatar *et al.* 2005) consists of three layers, inducing a 50 per cent relative change of the Young modulus. The shallowest layer is 8 km thick with low velocity (5.3 km s^{-1}), typical of sedimentary layer. The maximum coseismic slip occurred in that upper layer. This validates our assumption of a dislocation taking place within a uniform elastic half-space. By contrast, aftershocks are located deeper, in a higher velocity layer (6 km s^{-1}).

Considering this apparently clear distinction between aftershocks distribution and coseismic fault slip, we are faced again with the expected resolution of our models. NA models resolution for rupture boundaries at depth looked rather good (about 2 km), but within a very simple dislocation model (uniform slip on a rectangular fault patch, in a uniform elastic half-space). As for the least-square inversion process, we stated that the resolution below 5 km is very poor (few km). So, it is important to keep in mind, as suggested by (Tatar *et al.* 2005), that aftershocks and coseismic slip can still overlap significantly.

As seen before, aftershocks distribution and geodetic data provide similar fault location, but they may differ in the dip angle estimation. Aftershocks seismicity indicates a single plane, slightly dipping westward, whereas geodetic data suggest a slightly east dipping fault plane. In addition to uncertainties associated with each dip angle estimates, this apparent incompatibility can be solved if we consider that geodetic data mainly reflect shallow dislocation characteristics. Then, the rupture can have been initiated at depth

on the Bam-Baravat escarpment, and propagated towards the surface along the east-dipping fault branch. Indeed, as described by (ICG 2004), the Bam-Baravat escarpment and the new fault can be interpreted as a monocline above a steep reverse fault. We tested some dislocation models using such geometry, within a trial-error approach. However, they did not significantly reduce the misfit function between predicted and observed geodetic data. The inversion procedure presented in this paper should be extended to multifault segments geometry.

Aftershocks distribution confirms the main features of dislocation models derived from geodetic data, while adding some details at depth. Yet, this slip on planes underlying the seismogenic rupture can not be observed on post-seismic interferograms spanning 1 yr after the earthquake.

Finally, although all models presented in this paper lead to satisfactory misfit between predicted and observed surface deformation measurements, they never fit precisely all geodetic data sets. Significant residues can only be removed at the cost of higher residues on other data sets, or unrealistic roughness of the slip distribution. May be some more sophisticated data weighting strategies should be adopted, privileging for example offset and levelling data close to the fault, and InSAR data elsewhere. Furthermore, as suggested by aftershocks seismicity or dislocation models derived by least-square inversion technique, a more complex geometry could be considered. More steadily, though not suggested by inversion of traveltimes of aftershocks, a possible finer velocity structure (hence, spatial variation in elastic properties) could be taken into account. Using finite element modelling we tested the influence of a thin top layer with low rigidity on the predicted surface deformation. We observed that such a rheological model affects the predicted deformation at large scale but does not increase significantly the horizontal gradient of deformation in the vicinity of the fault. Conversely, compliant fault zone model associated to a significant reduction in the effective shear modulus close to the fault have been proposed (Fialko 2004). Although available seismic studies around the Bam fault have not shown such variations (Tatar *et al.* 2005), such lateral variation could explain that the models residues mainly occur in the near field of the fault.

7 CONCLUSION

Surface deformation induced by Bam earthquake has been precisely mapped by geodesy. We constructed ascending and descending Envisat ASAR interferograms, horizontal offset images on SPOT5 and Envisat ASAR images. We completed this data set with one differential levelling profile across the ruptured zone.

We present a new two-step inversion procedure. The first step consists in the determination of a simple dislocation model (uniform slip on a single plane fault) by use of the NA. This stage provides optimal models (10 parameters) with respect to some misfit function between predicted and observed data. This stochastic approach enables the appraisal of each parameter stability. Retaining the optimal geometry, a standard linearized weighted least square inversion technique is applied, in order to derive a detailed slip-distribution at depth. This two-step inversion procedure process geodetic data sets, either separately or jointly.

NA processing shows that InSAR data hold the most complete and reliable information but are significantly complemented by levelling and offsets measurements close to the rupture. The optimal model reveals a shallow (between 1 and 6 km) strike-slip motion, up to 2.0 m, on a slightly east-dipping fault.

The second inversion technique confirms the previous dislocation model main features, without improving significantly the overall data misfit. Our optimal model is characterized by a particular weighting of each geodetic data set and some smoothness applied to the slip distribution. The analysis of resolution matrices indicates that the detailed slip distribution accessible to the inversion process is limited to the very first kilometres at depth.

The aftershocks distribution is located just beneath the fault segment that, according to our models, experienced the maximum slip. It suggests a west-dipping fault at depth that could be interpreted as the Bam-Baravat escarpment on which the rupture could have been initiated. In order to interpret the remaining residues between predicted and observed surface deformation, more complex fault geometry should be considered, as well as possible low elastic compliance in the vicinity of the fault.

ACKNOWLEDGMENTS

We thank the European Space Agency for delivering Envisat SLC images, F. Sarti and R. Binet for providing us with offsets images. We are grateful to M. Sambridge for giving us access to the NA code, to A. Lovenbruck who provided us with a least-square inversion code adapted to GPS, and to R. Michel who developed the subpixel correlation method. We also thank two anonymous reviewers who provided constructive reviews of this paper.

REFERENCES

Aki, K., 1972. Earthquake mechanism, *Tectonophysics,* **13,** 423–446.

Ambraseys, N. & Melville, C., 1982. *A history of Persian earthquakes*, Cambridge Univ. Press, Cambridge, UK.

Archuleta, R.J., 1984. A faulting model for the 1979 Imperial Valley, California, earthquake, *J. geophys. Res.,* **89,** 4559–4585.

Archuleta, R.J., 1982. Analysis of near-source static and dynamic measurement from the 1979 Imperial Valley earthquake, *Bull. seism. Soc. Am.,* **72,** 1927–1956.

Arnadottir, T. & Segall, P., 1994. The 1989 Loma Prieta earthquake imaged from inversion of geodetic data, *J. geophys. Res.,* **99,** 21 835–21 855.

Arnadottir, T., Segall, P. & Matthews, M., 1992. Resolving the discrepancy between geodetic and seismic fault models for the 1989 Loma Prieta, California, earthquake, *Bull. seism. Soc. Am.,* **82,** 2248–2255.

Arnadottir, T., Segall, P. & Delaney, P.T., 1991. A fault model for the 1989 Kilauea south flank earthquake from leveling and seismic data, *Geophys. Res. Lett.,* **18,** 2217–2220.

Berberian, M. et al., 2001. The March 14 1998 Fandoqa earthquake (Mw 6.6) in Kerman province, SE Iran: re-rupture of the 1981 Sirch earthquake fault, triggering of slip on adjacent thrusts, and the active tectonics of the Gowk fault zone, *Geophys. J. Int.,* **146,** 371–398.

Berberian, M. & Yeats, R.S., 1999. Patterns of Historical Earthquake rupture in the Iranian Plateau, *Bull. seism. Soc. Am.,* **89,** 120–139.

Berberian, M., Jackson, J.A., Ghorashi, M. & Kadjar, M.H., 1984. Field and teleseismic observations of the 1981 Golbaf-Sirch earthquakes in SE Iran., *Geophys. J. R. astr. Soc.,* **77,** 809–838.

Binet, R. & Bollinger, L., 2005. Horizontal co-seismic deformation of the 2003 Bam (Iran) earthquake measured from Spot-5 THR satellite imagery, *Geophys. Res. Lett.,* **32**(2), doi:10.1029/2004GL021897.

Bos, A.G., Usai, S. & Spakman, W., 2004. A joint analysis of GPS motions and InSAR to infer the coseismic surface deformation of the Izmit, Turkey earthquake, *Geophys. J. Int.,* **158,** 849–863.

Bos, A.G. & Spakman, W., 2003. The resolving power of coseismic surface displacement data for fault slip distribution at depth, *Geophys. Res. Lett.,* **30**(21), 2110, doi:10.1029/2003GL017946.

Bouchon, M., Campillo, M. & Cotton, F., 1998. Stress field associated with the rupture of the 1992 Landers, California, earthquake and its

implications concerning the fault strength at the onset of the earthquake, *J. geophys. Res.,* **103,** 21 091–21 097.

Bürgmann, R. et al., 2002. Deformation during the 12 November 1999 Düzce, Turkey, Earthquake, from GPS and InSAR Data, *Bull. seismol. Soc. Am.,* **92,** 161–171.

Cervelli, P., Murray, M.H., Segall, P., Aoki, Y. & Kato, T., 2001. Estimating source parameters from deformation data, with an application to the March 1997 earthquake swarm off the Izu Peninsula, Japan, *J. geophys. Res.,* **106**(B6), 11 217–11 237.

Clarke, P.J., Paradissis, D., Briole, P., England, P.C., Parsons, B.E., Billiris, H., Veis, G. & Ruegg, J.C., 1997. Geodetic investigation of the 13 May 1995 Kozani - Grevena (Greece) earthquake, *Geophys. Res. Lett.,* **24**(6), 707–710.

Das, S. & Henry, C., 2003. Spatial relation between main earthquake slip and its aftershock distribution, *Rev. Geophys.,* **41,** 3/1–3/23.

Delouis, B., Giardini, D., Lundgren, P. & Salichon, J., 2002. Joint inversion of InSAR, GPS, teleseimic, and strong-motion data for the spatial and temporal distribution of earthquake slip: application to the 1999 Izmit mainshock, *Bull. seism. Soc. Am.,* **92,** 278–299.

Delouis, B., Lundgren, P., Salichon, J. & Giardini, D., 2000. Joint inversion of InSAR and teleseimic data for the slip history of the 1999 Izmit (Turkey) earthquake, *Geophys. Res. Lett.,* **27,**20, 3389–3392.

Du, Y., Segall, P. & Gao, H., 1994. Dislocation in inhomogeneous media via a moduli perturbation approach; general formulation and two-dimensional solutions, *J. geophys. Res.,* **99,** 13 767–13 779.

Du, Y., Aydin, A. & Segall, P., 1992. Comparison of various inversion techniques as applied to the determination of a geophysical deformation model for the 1983 Borah Peak earthquake, *Bull. seism. Soc. Am.,* **82,** 1840–1866.

Eberhart-Phillips, D. & Stuart, W.D., 1992. Mechanical heterogeneity simplifies the picture: Loma Prieta, *Bull. seism. Soc. Am.,* **82,** 1964–1968.

Feigl, K. et al., 2002. Estimating slip distribution for the Izmit mainshock from co-seismic GPS, ERS-1, RADARSAT and SPOT measurements, *Bull. seism. Soc. Am.,* **92,** 138–160.

Fialko, Y., Sandwell, D., Simons, M. & Rosen, P., 2005. Three-dimensional deformation caused by the Bam, Iran, earthquake and the origin of shallow skip deficit, *Nature,* **435**(19), 295–299.

Fialko, Y., 2004. Probing the mechanical properties of seismically active crust with space geodesy. Study of the coseismic deformation due to the 1992 Mw7.3 Landers (southern California) earthquake, *J. geophys. Res.,* **109,** doi:10.1029/2003JB002756.

Fielding, E.J., Talebian, M., Rosen, P.A., Nazari, H., Jackson, J.A., Ghoraishi, M. & Berberian, M., 2005. Surface ruptures and building damage of the 2003 Bam, Iran earthquake mapped by satellite SAR interferometry correlation, *J. geophys. Res.,* doi:10.1029/2004JB003299.

Funning, G.J., Parsons, B., Wright, T.J., Fielding, E.J. & Jackson, J.A., 2005. Surface displacements and source parameters of the 2003 Bam (Iran) earthquake from Envisat ASAR imagery, *J. geophys. Res.,* **110**(B9), doi:B0940610.1029/2004JB003338.

Gao, L. & Wallace, T.C., 1995. The 1990 Rudbar-Tarom Iranian earthquake sequence: Evidence for slip partitionning, *J. geophys. Res.,* **100**(B8), 15 317–15 332.

Ghiglia, D. & Romero, L., 1994. Robust two-dimensional weighted and unweighted phase unwrapping that uses fast transforms and iterative methods, *J. Opt. Soc. Am.,* **11**(1), 107–117.

Hartzell, S.H. & Heaton, T.H., 1983. Inversion of strong ground motion and telesismic waveform data for the rupture history of the 1979 Imperial Valley, California, earthquake, *Bull. seism. Soc. Am.,* **73,** 1553–1583.

Hearn, H.H. & Bürgmann, R., 2005. The effect of elastic layering on inversions of GPS data for coseismic slip and resulting stress changes: Strike-slip earthquakes, *Bull. seism. Soc. Am.,* **95,** 1637–1653.

Hernandez, B., Cotton, F. & Campillo, M., 1999. Contribution of radar interferometry to a two-step inversion of the kinematic process of the 1992 Landers earthquake, *J. geophys. Res.,* **104,** 13 083–13 099.

Hessami, K., Tabassi, H., Abbassi, M.R., Azuma, T., Okumura, K., Echigo, T. & Kondo, H., 2004. Surface expression of the Bam fault zone in southeast Iran: causative fault of the 26 December 2003 Bam earthquake, *J. Seism. Earthq. Eng.,* **4,** 5–14.

Hudnut, K.W. et al., 1994. Co-seismic displacements of the 1992 Landers earthquake, *Bull. seism. Soc. Am.,* **84,** 625–645.

ICG Reconnaissance Mission, 2004. Bam Earthquake of 26 December 2003, ICG Reconnaissance Mission, ICG report 2004–99-1.

Jackson, D.D., 1979. The use of a priori data to resolve non-uniqueness in linear inversion, *Geophys. J. R. astr. Soc.,* **57,** 137–157.

Jackson, J.A. & McKenzie, J., 1988. The relationship between plate motion and seismic moment tensors and the rate of active deformation in the Mediterranean and Middle East, *Geophys. J. R. astr. Soc.,* **93,** 45–73.

Jonsson, S., Zebker, H., Segall, P. & Amelung, F., 2002. Fault slip distribution of the 1999 Mw 7.1 Hector Mine, California, earthquake, estimated from satellite radar and GPS measurements, *Bull. seism. Soc. Am.,* **92,** 1377–1389.

Lohman, R.B., Simons, M. & Savage, B., 2002. Location and mechanism of the Little Skull Mountain earthquake as constrained by satellite radar interferometry and seismic waveform modeling, *J. geophys. Res.,* **107,** B6, doi:10.1029/2001JB00067.

Lovenbruck, A., Cattin, R., Le Pichon, X., Dominguez, S. & Michel, R., 2004. Coseismic slip resolution and postseismic relaxation time of the 1999 Chi-Chi, Taiwan, earthquake as constrained by geological observations, geodetic measurements and seismicity, *Geophys. J. Int.,* **158,** 310–326.

Memarzadeh, Y., 1998. Refraction effect and statistical analysis of the Iranian first order precise levelling data, *M.Sc. thesis*, Dep. of Surveying Engineering, K.N. Toosi University, Tehran, Iran

Michel, R. & Avouac, J.P., 2002. Deformation due to the 17 August 1999 Izmit Turkey, earthquake measured from SPOT images, *J. geophys. Res.,* **107,** 2062, doi:10.1029/2000JB000102.

Michel, R., Avouac, J.P. & Taboury, J., 1999. Measuring near field coseismic displacements from SAR images: application to the Landers earthquake, *Geophys. Res. Lett.,* **26**(19), 3017–3020.

Motagh, M., Klotz, J., Tavakoli, F., Djamour, Y., Arabi, S., Wetzel, H.U. & Zschau, J., 2006. Combination of precise leveling and InSAR data to constrain source parameters of the $M_w = 6.5$, 26 December 2003 Bam earthquake, *Pure appl. Geophys.,* **163,** 1–18, doi:10.1007/s00024–005-0005-y.

Nakamura, T. et al., 2005. Source fault structure of the 2003 Bam earthquake, southeastern Iran, inferred from the aftershock distribution and its relation to the heavily damaged area: existence of the Arg-e-Bam fault proposed, *Geophys. Res. Lett.,* **32,** L09308, doi:10.1029/2005GL022631.

Okada, Y., 1985. Surface deformation due to shear and tensile faults in a half-space, *Bull. seism. Soc. Am.,* **75,** 1135–1154.

Olson, A.H. & Apsel, R.J., 1982. Finite fault and inverse theory with applications to the 1979 Imperial Valley earthquake, *Bull. seism. Soc. Am.,* **72,** 1969–2001.

Pedersen, R., Jonsson, S., Arnadottir, T., Sigmundsson, F. & Feigl, K., 2003. Fault slip distribution of two June 2000 Mw 6.5 earthquakes in South Iceland estimated from joint inversion of InSAR and GPS measurements, *Earth planet. Sci. Lett.,* **213,** 487–502.

Pollitz, F.F., 1996. Coseismic deformation from earthquake faulting on a layered spherical Earth, *Geophys. J. Int.,* **125,** 1–14.

Rybicki, K., 1971. The elastic residual field of a very long strike-slip fault in the presence of a discontinuity, *Bull. seism. Soc. Am.,* **61,** 79–92.

Salichon, J., Delouis, B., Lundgren, P., Giardini, D., Costantini, M. & Rosen, P., 2003. Joint inversion of broadband teleseimic and interferometric synthetic aperture radar (InSAR) data for the slip history of the Mw=7.7, Nazca ridge (Peru) earthquake of 12 November 1996, *J. geophys. Res.,* **108**(B2), 2085, doi:10.1029/2001JB000913.

Sambridge, M., 1999a. Geophysical inversion with a neighbourhood algorithm - I. Searching a parameter space, *Geophys. J. Int.,* **138,** 479–494.

Sambridge, M., 1999b. Geophysical inversion with a neighbourhood algorithm—II. Appraising the ensemble, *Geophys. J. Int.,* **138,** 727–746.

Sarti, F., Briole, P. & Pirri, M., 2006. Co-seismic fault rupture detection and slip measurement by ASAR precise correlation using coherence maximisation. Application to a North-South blind fault in the vicinity of Bam (Iran), *IEEE Geosci. Remote Sens. Let.,* doi:10.1109/LGRS.2005.852475.

Savage, J.C., 1998. Displacement field for an edge dislocation in a layered half-space, *J. geophys. Res.,* **103,** 2539–2446.

Savage, J.C., 1987. Effect of crustal layering upon dislocation modeling, *J. geophys. Res.,* **92,** 10 595–10 600.

Scholtz, C.H., 1990. *The mechanics of earthquakes and faulting*, Cambridge Univ. Press, Cambridge, UK.

Simmons, M., Fialko, Y. & Rivera, L., 2002. Co-seismic static deformation from the 1999 Mw 7.1 Hector Mine, California, earthquake, as inferred from InSAR and GPS observations, *Bull. seism. Soc. Am.,* **92,** 1390–1402.

Talebian, M. et al., 2004. The 2003 Bam (Iran) earthquake rupture of 'truly blind' fault, *Geophys. Res. Lett.,* **31,**L11, 611 doi:10.1029/2004GL020,058.

Tarantola, A., 1987. *Inverse problem theory*, Elsevier, Amsterdam.

Tatar, M., Hatzfeld, D., Moradi, A.S. & Paul, A., 2005. The 26 December 2003 Bam Earthquake (Iran), Mw 6.6, aftershock sequence, *Geophys. J. Int.,* doi:10.1111/j.1365–246X.2005.02639.x

Vallée, M. & Bouchon, M., 2004. Imaging coseismic ruture in far field by slip patches, *Geophys. J. Int.,* **156,** 615–630.

Vernant, P. et al., 2004. Contemporary Crustal Deformation and Plate Kinematics in Middle East constrained by GPS measurements in Iran and Northern Oman, *Geophys. J. Int.,* **157,** 381–398.

Walker, R. & Jackson, J., 2002. Offset and evolution of the Gowk fault, S.E. Iran: a major intra-continental strike-slip system, *J. Struct. Geol.,* **24,** 1677–1698.

Wang, R., Xia, Y., Grosser, H., Wetzel, H.U., Kaufmann, H. & Zschau, J., 2005. The Mw=6.5 Bam (SE Iran) earthquake. Precise source parameters from satellite radar interferometry, *Geophys. J. Int.,* doi:101111/j.1365-246X.2004.02476.x

Wang, R., Martin, F.L. & Roth, F., 2003. Computation of deformation induced by earthquakes in a multi layered elastic crust— Fortran programs EDGRN/EDCMR, *Comp. Geosci.,* **29,** 195–207.

Ward, S.N. & Barrientos, S., 1986. An inversion for slip distribution and fault shape from geodetic observations of the 1983, Borah Peak, Idaho, earthquake, *J. geophys. Res.,* **91,** 4909–4919.

Wright, T.J., Parsons, B.E., Jackson, J.A., Haynes, M., Fielding, E.J., England, P.C. & Clarke, P.J., 1999. Source parameters of the 1 October 1995 Dinar (Turkey) earthquake from SAR interferometry and seismic body wave modeling, *Earth planet. Sci. Lett.,* **172,** 23–27.

Zhao, S., Muller, R., Takahashi, Y. & Kaneda, Y., 2004. 3D finite element modeling of deformation and stress associated with faulting: effect of inhomogeneous crustal structures, *Geophys. J. Int.,* **157,** 629–644.